Check for updates

Terahertz time-domain spectroscopy of zone-folded acoustic phonons in 4H and 6H silicon carbide

ABEBE T. TAREKEGNE,[1] BINBIN ZHOU,[1] KORBINIAN KALTENECKER,[1] KRZYSZTOF IWASZCZUK,[2] STEWART CLARK,[3] AND PETER UHD JEPSEN[1,*]

[1]*DTU Fotonik - Department of Photonics Engineering, Technical University of Denmark, Kongens Lyngby DK-2800, Denmark*
[2]*NKT Photonics A/S, Blokken 84, Birkerød DK-3460, Denmark*
[3]*Department of Physics, University of Durham, South Road, Durham DH1 3LE, UK*
*puje@fotonik.dtu.dk

Abstract: We investigate the dielectric properties of the 4H and 6H polytypes of silicon carbide in the 0.1-19 THz range, below the fundamental transverse-optical phonons. Folding of the Brillouin zone due to the specific superlattice structure of the two polytypes leads to activation of acoustic phonon modes. We use a combination of ultrabroadband terahertz time-domain spectroscopy and simulations based on density-functional perturbation theory to observe and characterize these modes, including band splitting due to the dissimilar carbon and silicon sublattices of the structures, and an indirect measurement of the anisotropic sound velocities in the two polytypes.

1. Introduction

Silicon carbide (SiC) is an important material for power electronics and optoelectronics due to its uniquely high dielectric strength, high bandgap, and mechanical hardness [1,2]. Recently, SiC has attracted attention as host material for solid-state single photon emitters [3] as well as dielectric substrate material for graphene growth [4,5], nanophotonics at long wavelengths with surface phonon polaritonics [6], mid-IR femtosecond pulse generation [7], and THz generation in the difficult-to-access 5-15 THz region [8]. Natural SiC superlattices can emit THz electroluminescence due to Bloch oscillations [9], and it was recently demonstrated that high-quality graphene nanoribbons with ballistic electron on the μm scale at room temperature can be grown on sidewalls of SiC mesas [10,11].

It is well known that SiC naturally forms a wide range of polytypes, depending on the stacking sequence of the individual SiC layers of the material. Stacking increases the size of the crystal unit cell in the growth direction compared to the simple cubic SiC unit cell (3C SiC), and thus reduces the size of the Brillouin zone (BZ) correspondingly. This reduction can be understood as a folding of the cubic BZ, and therefore the edges of the simple BZ are projected onto the center of the BZ of the given polytype (see e.g [12,13].). The same zone-folding effect is also observed in artificial superlattice structures, such as GaAs/AlAs [14] and GaSe [15]. Here we perform a detailed investigation of the infrared active zone-folded acoustic phonons below the TO frequency in the most common polytypes 4H and 6H of SiC that are commercially available in wafer dimensions. The acoustic phonons in these and other polytypes have been studied extensively by Raman spectroscopy [12,13], and their nature is well established. However, these exceedingly weak modes are not obvious in infrared spectroscopy, and have not been characterized in recent studies of the optical properties of SiC in the same spectral range [8,16]. To the best of our knowledge, the modes have not been observed and documented in IR spectroscopy with the exception of the LA mode in 6H SiC [17].

2. Experimental details and samples

Measurements were performed by THz time-domain spectroscopy, realized by two-color femtosecond air plasma THz generation in the focal region of the fundamental output and its second harmonic from a femtosecond Ti:sapphire amplifier system (35 fs FWHM pulse length, 800 nm central wavelength, $f_0 = 1$ kHz repetition rate), as shown in Fig. 1. The resulting THz pulses are quasi-single cycle signals with a <35 fs FWHM duration of the central oscillation, covering the spectral region 1-30 THz with a smooth spectrum (see insets in Fig. 2). The THz pulse propagates through a set of off-axis paraboloidal mirrors through an intermediate focus, and into the detection region, where air biased coherent detection (ABCD) [18,19] was used for detection, with modulation of the local oscillator bias (V_{loc}) locked at $f_0/2$ (see Fig. 1).
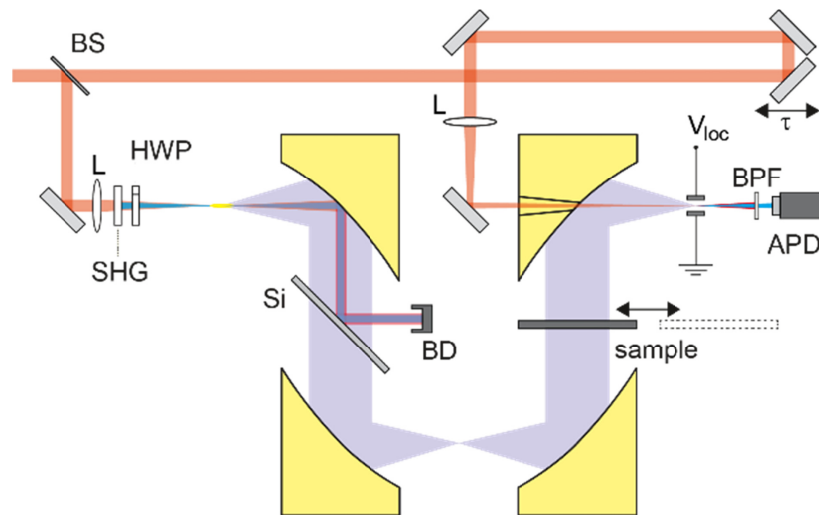
Fig. 1. Experimental setup. BS – R/T 80/20 beamsplitter; SHG – second harmonic generation crystal; HWP – dual wavelength half-wave plate; Si – silicon plate; BD – beam dump; BPF – 400-nm band pass filter; APD – avalanche photodiode; L – focusing lenses. The setup is driven by 35-fs, 800 nm, 1.5 mJ laser pulses at 1 kHz repetition rate.

The samples were vanadium-compensated, semi-insulating ($\rho > 10^{11}$ ohm·cm) 4H and 6H SiC (supplied by II-VI Advanced Materials, Inc.) with 10 cm diameter and thicknesses 491 and 502 µm, respectively, measured by a calibrated micrometer caliper. The crystal lattice of both polytypes is hexagonal (C_{6v}), with the (0001) face in the plane of the wafer. Following the standard nomenclature, the 4H and 6H polytypes have stacking sequences ABCB and ABCACB, respectively. Optical measurements performed normal to the surface were performed to probe the ordinary index of refraction and transverse (planar) phonon modes. All measurements were performed with the sample in a collimated section of the THz beam path in order to avoid artifacts by the Gouy phase shift in the focal region [20].

3. Experimental data

Figure 2 shows the raw time-domain signals. The black and red curves represent the reference and sample signals, respectively, for transmission through 4H and 6H SiC. The insets show the amplitude spectra of the signals on a logarithmic scale. The reference signal has a bandwidth extending beyond 30 THz, and the signal through SiC is cut off at 19 THz due to strong absorption by the fundamental transverse optical (TO) phonon. The signals were recorded with a temporal resolution of 6.7 fs (1 µm step size on the translation stage) over a time window of approximately 10 ps. During subsequent data analysis, the signals

were zero-padded by a factor 4. Each data set is averaged from two individual time traces, with an acquisition time of approximately 8 minutes per trace (100 ms lock-in time constant).

Prominent time-domain ringing patterns is seen in both cases, indicative of the strong dispersion of the material and additional sharp absorption bands within the signal bandwidth. The zoom-in regions in the insets show these additional absorption features, located at 7.9 THz in 4H and 7-7.1 THz in 6H SiC, respectively.
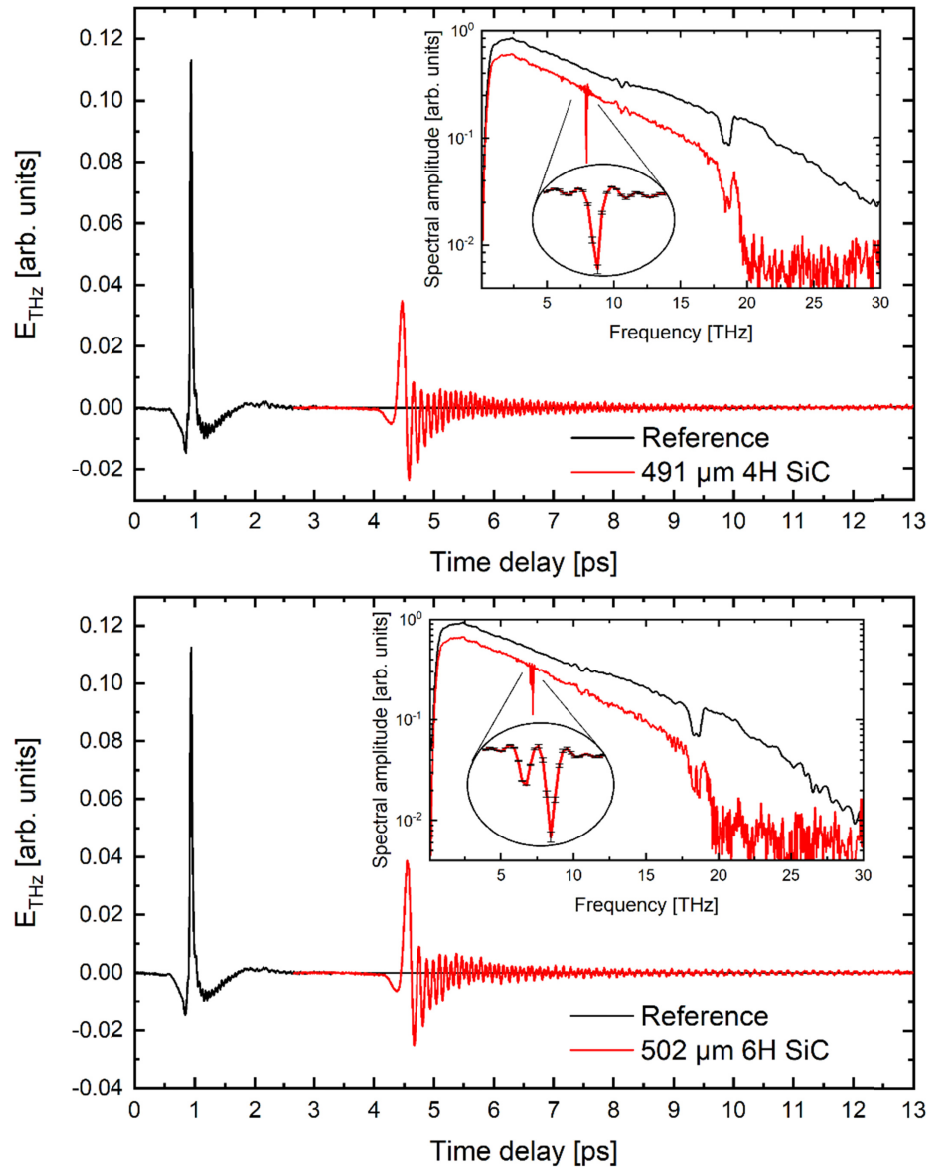
Fig. 2. Time-domain THz electric field transients (reference: black; sample: red) for (a) 4H SiC and (b) 6H SiC. Insets show the spectral amplitudes of each trace, with zoom on the narrow resonance features. Error bars indicate the standard deviation of 5 sequential measurements of each sample.

The amplitude ratio A_{sam} / A_{ref} and phase difference $\Delta\phi$ between the sample (direct pass) and reference spectra are used in the standard manner to extract the index of refraction n and

extinction coefficient κ [21]. The complex permittivity is then determined as $\tilde{\varepsilon} = (n + i\kappa)^2$. Figures 3(a) and 3(b) show the real and imaginary parts of the permittivity of the two polytypes across the 1-19 THz band, measured at normal incidence, with insets showing a zoom onto the weak but sharp spectral bands in the 7-8 THz range, due to transverse acoustic phonons activated by zone folding. The black, dashed curves are global fits to the real and imaginary parts of the experimental permittivity data with a multi-Lorentzian function,

$$\varepsilon(\omega) = \varepsilon_\infty + \sum_k \frac{W_k}{\omega_{0,k}^2 - \omega^2 - i\omega/\tau}, \tag{1}$$

taking into account both the strong fundamental TO phonon that is responsible for the general dispersion across the frequency range explored here, and the weak polytype-specific modes in the 7-8 THz range. The resulting fit parameters are shown in Table 1. It can be noted that the zone-folded modes have intensities that are between 7 and 25 parts per million relative to the strong TO phonon. Although outside the range of the spectroscopic data, the position of the TO phonon can easily be obtained from the fits due to the strong dispersion of the real part of the permittivity at lower frequencies.

Figure 3(c) shows the imaginary part of the permittivity of both polytypes, measured at 70° incidence angle, resulting in an internal propagation angle of 14.5° and giving access to the extraordinary axis of the refractive index. The high angle of incidence leads to slight shift of the THz beam path, so quantitative spectroscopic information is difficult to extract. However, we observe narrow absorption bands at 18.3 and 15.2 THz in 4H and 6H SiC, respectively. These peaks are not observed at normal incidence (Fig. 3(b)), and are due to longitudinal acoustic phonons, as will be discussed below.

Table 1. Lorentzian fitting parameters for 4H and 6H SiC

Parameter, units	4H SiC	6H SiC
ε_∞	6.587 ± 0.003	6.625 ± 0.003
W_1 [ps^{-1}]	1.72 ± 0.04	0.52 ± 0.06
W_2 [ps^{-1}]	-	1.85 ± 0.03
W_3 [ps^{-1}]	71734 ± 84	71342 ± 87
τ_1 [ps]	9.4 ± 0.4	4.0 ± 0.8
τ_2 [ps]	-	12.4 ± 0.5
τ_3 [ps]	2.45 ± 0.03	2.61 ± 0.04
$\omega_{0,1}/2\pi$ [THz]	7.955 ± 0.001	7.034 ± 0.005
$\omega_{0,2}/2\pi$ [THz]	-	7.203 ± 0.001
$\omega_{0,3}/2\pi$ [THz]	23.92 ± 0.005	23.87 ± 0.005

Based on our experimental data, the relations for the ordinary refractive index of the two polytypes are

$$n_{o,4H}^2 = 6.588 + \frac{3.174 \cdot \lambda^2}{\lambda^2 - 157.1}, \tag{2}$$

$$n_{o,6H}^2 = 6.649 + \frac{3.152 \cdot \lambda^2}{\lambda^2 - 158.0}, \tag{3}$$

where λ is the wavelength in units of μm. The deviation between these relations and our experimental data is shown in the top panel of Fig. 4. The RMS deviation is well below 10^{-3} in the 15-300 μm range, excluding the narrow region of the folded-zone phonon modes that are not accounted for by the Sellmeier relations. For comparison, we show the excellent agreement with previous values for 4H SiC in the same spectral region obtained by Fischer *et al.* [8] and Naftaly *et al.* [16]
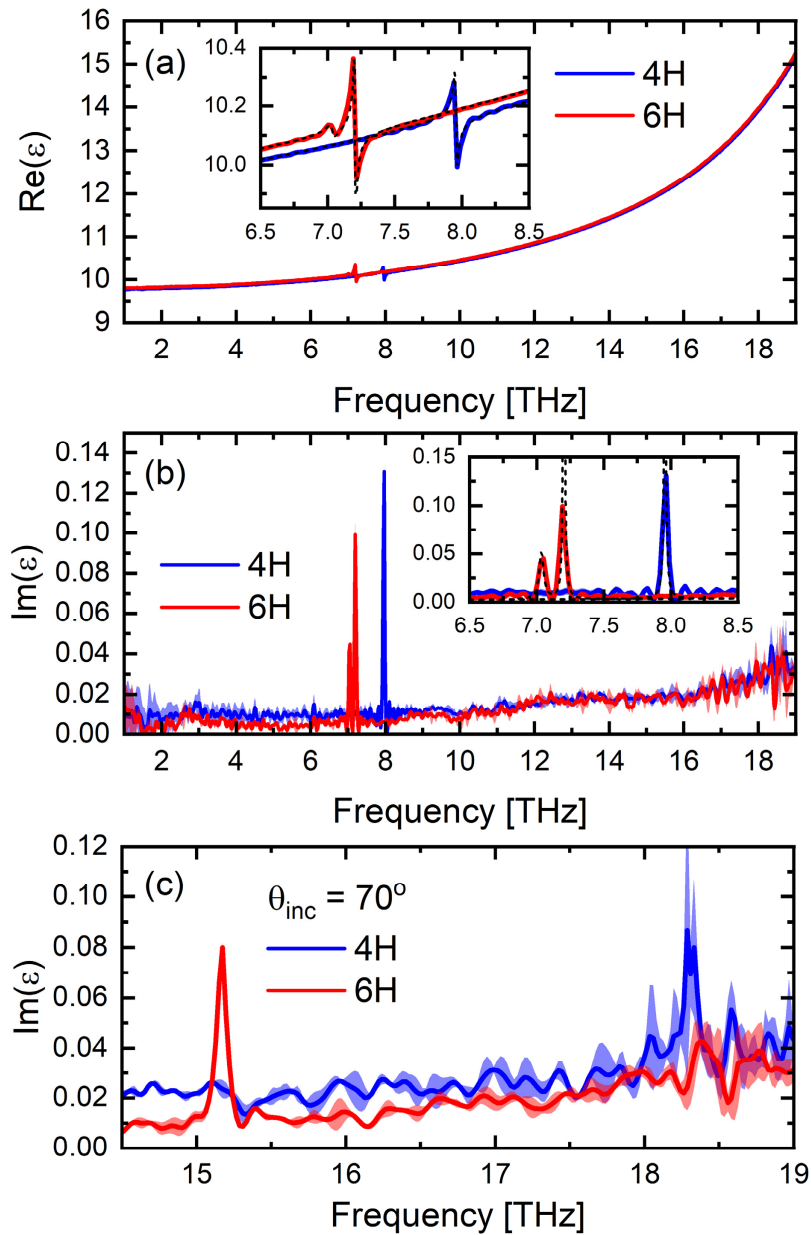
Fig. 3. (a) Real and (b) imaginary part of the permittivity of 4H (blue curves) and 6H (red curves) SiC. The insets show a zoom onto the resonant modes in the 6.5-8.5 THz region. Dashed curves in insets are Lorentz fits to the measurements. (c) Imaginary part of permittivity measured at 70 degrees incidence angle with longitudinal phonons at 18.4 THz (4H) and 15.2 THz (6H). The shaded areas around each curve indicate the standard deviation of the measurements.
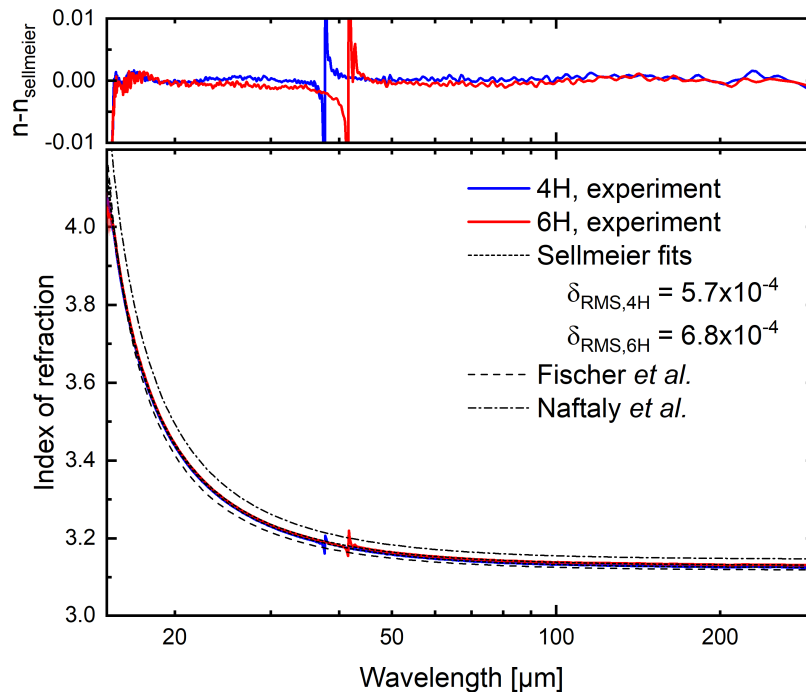
Fig. 4. Index of refraction of 4H (blue) and 6H (red) SiC (ordinary axis) as function of wavelength, together with Sellmeier fits in the range 15-300 µm. Shaded areas indicate standard deviation of the experimental data. Top panel shows deviation between experimental data and fits, with RMS deviations indicated in the legend. Dashed and dashed-dotted curves show the Sellmeier fits from [8,16], respectively (4H SiC).

4. Theoretical analysis

The nature of the observed sharp bands can be understood by considering phonons in the simplest cubic (3C) polytype. Here the phonon dispersion consist of two acoustic (TA and LA) and two optical (TO and LO) branches, where only the TO mode at wavevector $q = 0$ is infrared active. The phonon dispersion diagram of the higher polytypes can be qualitatively constructed by appropriate folding of the dispersion diagram along the stacking direction. The acoustic branches of the dispersion diagram are shown in Fig. 4(a) for 4H and Fig. 4(b) 6H polytypes. The dispersion diagram was calculated by ab-initio density functional perturbation theory (DFPT) as implemented in the Castep code [22,23] on optimized unit cells, using the exchange correlation functional PBEsol, a plane-wave energy cut-off of 1200 eV, $2.2 \cdot 10^{-10}$ eV/atom tolerance in electronic minimization, 10^{-5} eV/Å^2 phonon energy tolerance, and 10^{-5} Å^3 electric field convergence tolerance. A k point grid of 9x9x2 (total of 81 k points used after symmetry considerations). Figure 5 shows the resulting phonon dispersion curves of the transverse (red) and longitudinal (blue) acoustic phonon branches of (a) 4H and (b) 6H SiC. The IR intensities of the modes at $q = 0$ are indicated by gray bars (logarithmic scale).
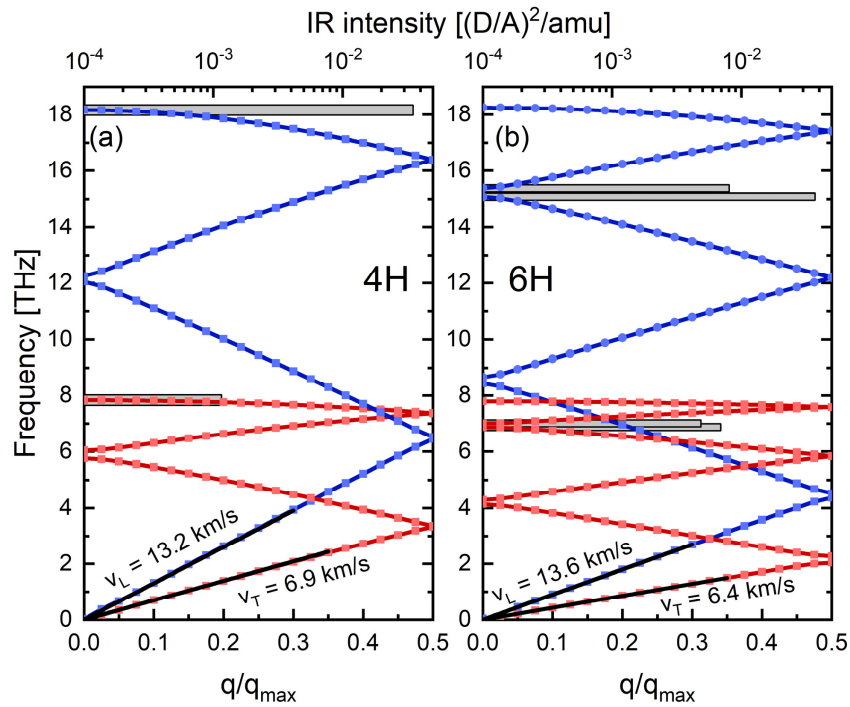
Fig. 5. Acoustic phonon dispersion diagrams of (a) 4H and (b) 6H SiC, calculated by DFT. Red and blue symbols represent transverse and longitudinal zone-folded acoustic branches, respectively. Grey bars indicate IR intensities (upper logarithmic scale) predicted by DFPT. Solid, black lines indicate the linear dispersion relation and speed of sound for the transverse and longitudinal directions.

The zone folding results in IR activation of several of the acoustic modes. In 4H SiC, a doubly degenerate TA mode and an LA mode is predicted, and in 6H SiC, two TA modes two LA modes are predicted, together with the strong TO phonon in both polytypes. The predicted frequencies are shown in Table 2, with a direct comparison to the experimentally determined frequencies in Fig. 3. The DFT frequencies are immediately confirmed by the experimental spectra shown in Fig. 3, with all deviations below 3% and an RMS deviation of only 0.5%.

Table 2. Experimental and DFT phonon frequencies [THz]

4H	Exp.	DFT	Δ [%]	6H	Exp.	DFT	Δ [%]
TA	7.96	7.83	1.6	TA	7.03	6.87	2.3
					7.20	7.00	2.8
LA	18.20	18.17	0.2	LA	15.2	15.1	0.7
						15.4	−1.3
TO	23.92	23.91	0.04	TO	23.87	23.86	0.04

The very good agreement between the theoretical and observed frequencies may at first glance be surprising. The DFPT calculation is performed at absolute zero temperature, and thus excludes anharmonic temperature effects such as redshift of frequencies and thermal expansion of the lattice, known to have significant influence on vibrational modes in crystalline materials in the THz range [24]. Figure 6 shows the calculated vibrational potential as function of the normal mode coordinates of the two motions for the 4H SiC TA mode and the upper of the 6H SiC TA modes (7.83 and 7.00 THz, respectively). The normal mode coordinates are scaled so that the curvature of the potential energy corresponds to the vibrational frequencies of the modes. The solid symbols represent the DFT potential energies, and the dashed curves represent simple harmonic fits that hardly deviates from the

DFT potential within the shown range, up to energies well above 1 eV. The thermal expansion coefficients of SiC are very low, with an estimated volume expansion of 6H SiC of $\Delta V / V_0 \approx 1.5 \cdot 10^{-9}$ between 0 and 300 K [25]. Pressure studies of SiC determined the shift of the TO phonon frequency to be $\Delta v_{TO} / (\Delta V / V_0) \approx 19\,\text{THz}$ [26], so the TO frequency shift due to thermal expansion alone between 0 and 300 K would be in the 30 kHz range, which can be safely ignored here. Thus, the harmonic vibrational potential indicates that the vibrational frequencies should be virtually independent of temperature.
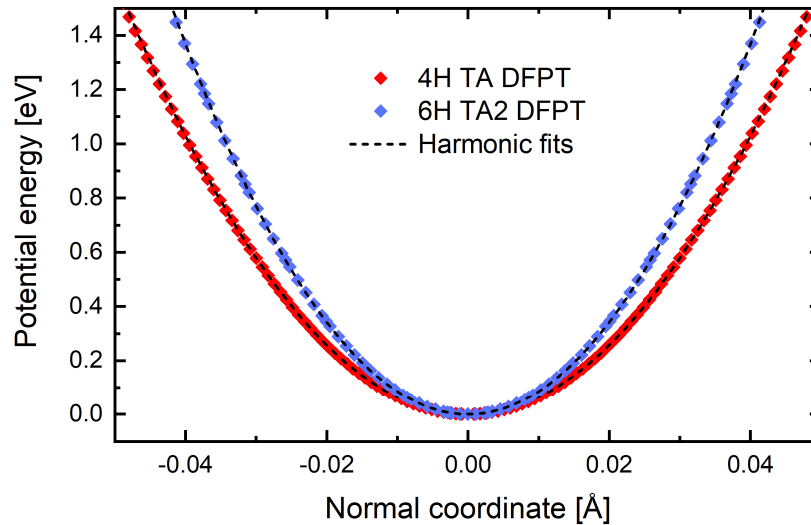
Fig. 6. Representative potential energy curves calculated by DFPT for the 4H SiC TA mode at 7.83 THz (red symbols) and the second 6H TA mode at 7.00 THz (blue symbols). Dashed lines are harmonic fits.

The precise agreement between experimental and theoretical frequencies of the IR active acoustic modes confirm the general shape of the calculated dispersion curves, and thus it is possible to accurately estimate the axial and planar sound velocities ($v = \omega/q$) in the 4H and 6H polytypes, as shown in Table 3.

Table 3. Planar (v_T) and axial (v_L) sound velocities (km/s) in 4H and 6H SiC, compared with literature values.

	6H	4H	6H [27]	4H [27]	6H [28]
v_T	6.4 ± 0.06	6.9 ± 0.07	7.1	7.0	7.3
v_L	13.6 ± 0.14	13.2 ± 0.13	13.1	13.0	13.3

The values are consistent with theoretical and experimental literature values [12,27,28], although our reported planar sound velocities are slightly lower than reported literature values. The low-frequency slope of the dispersion curves are uniquely defined by the frequencies of the IR activated acoustic modes, so we estimate the uncertainty of the extracted sound velocities to be given by the differences between optimized lattice constants in the simulation (mainly the c axis) and the experimental value at room temperature. The room temperature axial lattice parameter (*c* direction) for 4H and 6H SiC is 10.082 and 15.115 Å, respectively [29], and our optimized DFT unit cell parameters are 9.97 and 14.958 Å, respectively, which is 1% lower than the experimental values. This results in a similar relative uncertainty on the absolute slope of the dispersion curves in Fig. 5, and thus on the extracted sound velocities.

The detailed nature of the observed modes is detailed in Fig. 7, where we show the calculated eigenmotions of the individual ions in the unit cells, projected onto the transient dipole moment of each mode.
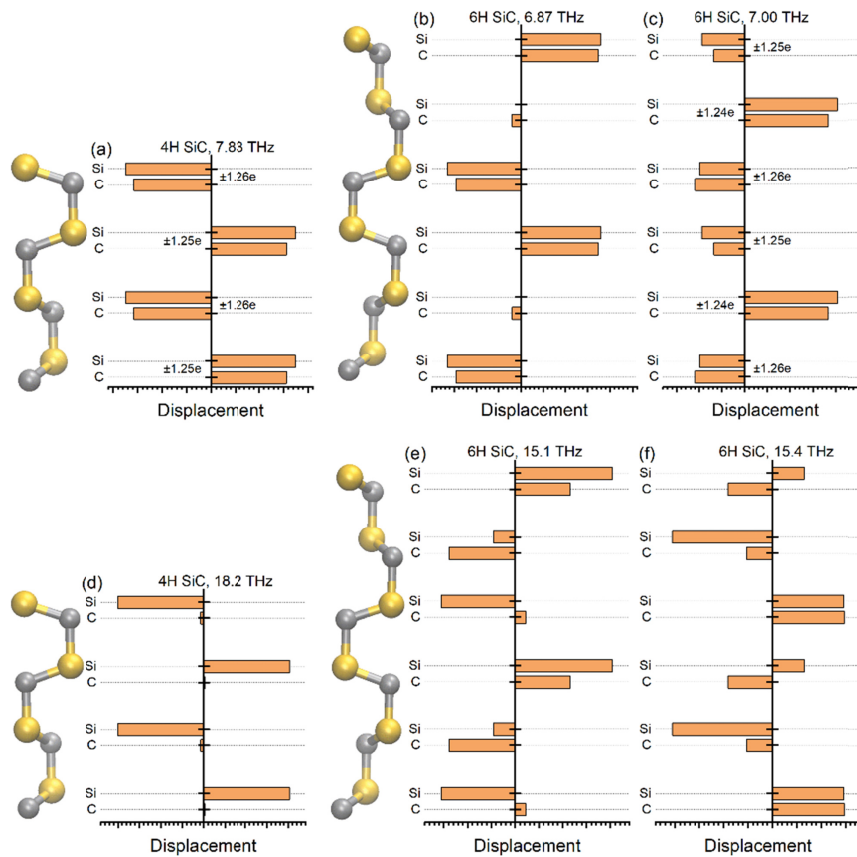
Fig. 7. Eigenmode motion of the zone-folded transverse (a-c) and longitudinal (d-f) acoustic modes of 4H SiC at 7.8 and 18.2 THz (a + d) and the split 6H SiC modes at 6.87 + 7.00 THz (b + c) and 15.1 + 15.4 THz (e + f). The bars indicate amplitude and polarization of the motion of the individual ions in the unit cell. See also Visualization 1, Visualization 2, Visualization 3, Visualization 4, Visualization 5, Visualization 6 **(1: 4H TA; 2: 6H TA1; 3: 6H TA2; 4: 4H LA; 5: 6H LA1; 6: 6H LA2)**.

The Si and C ions are positively and negatively charged, respectively. The total charge of each layer balances exactly, but there are small charge differences between the individual Si-C layers, as indicated in Figs. 7(a) and 7(c) for 4H and 6H SiC, respectively. These differences are due to the slightly different environments of the ions in the stacking layers of the polytypes. The transverse modes (Figs. 7(a)-7(c)) are rather clean acoustic modes, with the Si-C layers acting approximately as rigid units. The longitudinal modes (Figs. 7(d-7(f)) are, in comparison, less simple to describe. The 4H LA mode at 18.2 THz involves only motion if the Si ions, and is IR active mainly due to the minor charge differences between the layers. The 6H longitudinal modes are combinations of motion within each Si-C layer and semi-rigid interplane motion. Visualization sequences that illustrate the eigenmode motion of the folded TA and LA modes of the two polytypes are available as supplementary multimedia files (Visualization 1, Visualization 2, Visualization 3, Visualization 4, Visualization 5, Visualization 6, corresponding to the modes in Fig. 7(a)-7(f)).

5. Conclusion

We have used THz air photonics and air-biased coherent detection to measure the dielectric properties of the 4H and 6H polytypes of silicon carbide in the frequency range 1-19 THz, and observed the acoustic phonons activated by zone folding. We compared the observed

frequencies with predictions from density functional perturbation theory, and found excellent agreement, with 0.5% RMS deviation between observed and calculated frequencies. The zone-folded acoustic modes are very weak compared to the transverse optical phonon (by a factor of approximately 10^5), and we believe that the present study represents the first documented observation of these modes in infrared spectroscopy. The theoretical analysis allowed us to extract good estimates of the axial and planar sound velocities in both polytypes that are consistent with previous observations and calculations, and with a precision determined by the accuracy of the calculated vibrational frequencies.

Acknowledgments

References

1. T. Kimoto, and J. A. Cooper, *Fundamentals of silicon carbide technology* (John Wiley & Sons Singapore Pte. Ltd, 2014).
2. H. Ou, Y. Ou, A. Argyraki, S. Schimmel, M. Kaiser, P. Wellmann, M. K. Linnarsson, V. Jokubavicius, J. Sun, R. Liljedahl, and M. Syväjärvi, "Advances in wide bandgap SiC for optoelectronics," Eur. Phys. J. B **87**(3), 58 (2014).
3. I. Aharonovich, D. Englund, and M. Toth, "Solid-state single-photon emitters," Nat. Photonics **10**(10), 631–641 (2016).
4. K. V. Emtsev, A. Bostwick, K. Horn, J. Jobst, G. L. Kellogg, L. Ley, J. L. McChesney, T. Ohta, S. A. Reshanov, J. Röhrl, E. Rotenberg, A. K. Schmid, D. Waldmann, H. B. Weber, and T. Seyller, "Towards wafer-size graphene layers by atmospheric pressure graphitization of silicon carbide," Nat. Mater. **8**(3), 203–207 (2009).
5. J. Baringhaus, M. Ruan, F. Edler, A. Tejeda, M. Sicot, A. Taleb-Ibrahimi, A.-P. Li, Z. Jiang, E. H. Conrad, C. Berger, C. Tegenkamp, and W. A. de Heer, "Exceptional ballistic transport in epitaxial graphene nanoribbons," Nature **506**(7488), 349–354 (2014).
6. J. D. Caldwell, L. Lindsay, V. Giannini, I. Vurgaftman, T. L. Reinecke, S. A. Maier, and O. J. Glembocki, "Low-loss, infrared and terahertz nanophotonics using surface phonon polaritons," Nanophotonics **4**(1), 44–68 (2015).
7. H.-T. Fan, C.-H. Xu, Z.-H. Wang, G. Wang, C.-J. Liu, J.-K. Liang, X.-L. Chen, and Z.-Y. Wei, "Generation of broadband 17-μJ mid-infrared femtosecond pulses at 3.75 μm by silicon carbide crystal," Opt. Lett. **39**(21), 6249–6252 (2014).
8. M. P. Fischer, J. Bühler, G. Fitzky, T. Kurihara, S. Eggert, A. Leitenstorfer, and D. Brida, "Coherent field transients below 15 THz from phase-matched difference frequency generation in 4H-SiC," Opt. Lett. **42**(14), 2687–2690 (2017).
9. V. I. Sankin, A. V. Andrianov, A. O. Zakhar'in, and A. G. Petrov, "Terahertz electroluminescence from 6H-SiC structures with natural superlattice," Appl. Phys. Lett. **100**(11), 111109 (2012).
10 M. Kruskopf, D. M. Pakdehi, K. Pierz, S. Wundrack, R. Stosch, M. Dziomba, M. Gotz, J. Baringhaus, J. Aprojanz, C. Tegenkamp, J. Lidzba, T. Seyller, F. Hohls, F. J. Ahlers, and H. W. Schumacher, "Comeback of epitaxial graphene for electronics: large-area growth of bilayer-free graphene on SiC," 2D Mater. **3**, 041002 (2016).
11. J. Aprojanz, S. R. Power, P. Bampoulis, S. Roche, A.-P. Jauho, H. J. W. Zandvliet, A. A. Zakharov, and C. Tegenkamp, "Ballistic tracks in graphene nanoribbons," Nat. Commun. **9**(1), 4426 (2018).
12. D. W. Feldman, J. H. Parker, W. J. Choyke, and L. Patrick, "Phonon dispersion curves by Raman scattering in SiC, polytypes *3C, 4H, 6H, 15R*, and *21R*," Phys. Rev. **173**(3), 787–793 (1968).
13. S. Nakashima and H. Harima, "Raman investigation of SiC polytypes," Phys. Status Solidi, A Appl. Res. **162**(1), 39–64 (1997).
14. A. S. Barker, J. L. Merz, and A. C. Gossard, "Study of zone-folding effects on phonons in alternating monolayers of GaAs-AlAs," Phys. Rev. B Condens. Matter **17**(8), 3181–3196 (1978).
15. A. Polian, K. Kunc, and A. Kuhn, "Low-frequency lattice vibrations of δ-GaSe compared to ϵ- and γ-polytypes," Solid State Commun. **19**(11), 1079–1082 (1976).
16. M. Naftaly, J. F. Molloy, B. Magnusson, Y. M. Andreev, and G. V. Lanskii, "Silicon carbide--a high-transparency nonlinear material for THz applications," Opt. Express **24**(3), 2590–2595 (2016).
17. B. Ellis and T. S. Moss, "The conduction bands in 6H and 15R silicon carbide. II. Absorption measurements," Proc. R. Soc. Lond. A Math. Phys. Sci. **299**, 393–404 (1967).
18. J. Dai, X. Xie, and X. C. Zhang, "Detection of broadband terahertz waves with a laser-induced plasma in gases," Phys. Rev. Lett. **97**(10), 103903 (2006).

19. T. Wang, K. Iwaszczuk, E. A. Wrisberg, E. V. Denning, and P. U. Jepsen, "Linearity of Air-Biased Coherent Detection for Terahertz Time-Domain Spectroscopy," J. Infrared Millim. Terahertz Waves **37**(6), 592–604 (2016).
20. P. Kužel, H. Němec, F. Kadlec, and C. Kadlec, "Gouy shift correction for highly accurate refractive index retrieval in time-domain terahertz spectroscopy," Opt. Express **18**(15), 15338–15348 (2010).
21. P. U. Jepsen, D. G. Cooke, and M. Koch, "Terahertz spectroscopy and imaging – Modern techniques and applications," Laser Photonics Rev. **5**(1), 124–166 (2011).
22. S. J. Clark, M. D. Segall, C. J. Pickard, P. J. Hasnip, M. J. Probert, K. Refson, and M. C. Payne, "First principles methods using CASTEP," Z. Kristallogr. **220**, 567–570 (2005).
23. K. Refson, P. R. Tulip, and S. J. Clark, "Variational density-functional perturbation theory for dielectrics and lattice dynamics," Phys. Rev. B Condens. Matter Mater. Phys. **73**(15), 155114 (2006).
24. M. Walther, B. M. Fischer, and P. U. Jepsen, "Noncovalent intermolecular forces in polycrystalline and amorphous saccharides in the far infrared," Chem. Phys. **288**(2-3), 261–268 (2003).
25. Z. Li and R. C. Bradt, "Thermal expansion of the hexagonal (6H) polytype of silicon carbide," J. Am. Ceram. Soc. **69**(12), 863–866 (1986).
26. B. H. Cheong, K. J. Chang, and M. L. Cohen, "Pressure dependences of band gaps and optical-phonon frequency in cubic SiC," Phys. Rev. B Condens. Matter **44**(3), 1053–1056 (1991).
27. K. Kamitani, M. Grimsditch, J. C. Nipko, C.-K. Loong, M. Okada, and I. Kimura, "The elastic constants of silicon carbide: A Brillouin-scattering study of 4H and 6H SiC single crystals," J. Appl. Phys. **82**(6), 3152–3154 (1997).
28. G. Arlt and G. R. Schodder, "Some elastic constants of silicon carbide," J. Acoust. Soc. Am. **37**(2), 384–386 (1965).
29. M. Stockmeier, R. Müller, S. A. Sakwe, P. J. Wellmann, and A. Magerl, "On the lattice parameters of silicon carbide," J. Appl. Phys. **105**(3), 033511 (2009).